J. Fluid Mech. (2009), *vol.* 633, *pp.* 381–409.
doi:10.1017/S0022112009006983 Printed in the United Kingdom

Controlled impact of a disk on a water surface: cavity dynamics

RAYMOND BERGMANN†, DEVARAJ VAN DER MEER‡, STEPHAN GEKLE, ARJAN VAN DER BOS AND DETLEF LOHSE

Department of Applied Physics and J. M. Burgers Centre for Fluid Dynamics, University of Twente, PO Box 217, 7500 AE Enschede, The Netherlands

(Received 31 March 2008 and in revised form 20 February 2009)

In this paper we study the transient surface cavity which is created by the controlled impact of a disk of radius h_0 on a water surface at Froude numbers below 200. The dynamics of the transient free surface is recorded by high-speed imaging and compared to boundary integral simulations giving excellent agreement. The flow surrounding the cavity is measured with high-speed particle image velocimetry and is found to also agree perfectly with the flow field obtained from the simulations.

We present a simple model for the radial dynamics of the cavity based on the collapse of an infinite cylinder. This model accounts for the observed asymmetry of the radial dynamics between the expansion and the contraction phases of the cavity. It reproduces the scaling of the closure depth and total depth of the cavity which are both found to scale roughly as $\propto Fr^{1/2}$ with a weakly Froude-number-dependent prefactor. In addition, the model accurately captures the dynamics of the minimal radius of the cavity and the scaling of the volume V_{bubble} of air entrained by the process, namely, $V_{bubble}/h_0^3 \propto (1 + 0.26Fr^{1/2})Fr^{1/2}$.

1. Introduction

A spectacular example of free surface flow is the impact of an object on a liquid: the impact creates a splash and a transient cavity. This surface cavity then violently collapses under the influence of the hydrostatic pressure. At the singularity where the walls of the cavity collide, two powerful jets develop, one downwards and the other one upwards up to several metres high, making this fast event an impressive scene. Research into the physics of these transient surface cavities started at the beginning of the 20th century when A. M. Worthington published his famous work 'A study of splashes' (Worthington 1908). His photographs revealed a wealth of phenomena of unanticipated complexity (Worthington & Cole 1897). Although much has been contributed to the understanding of these phenomena, many of the intriguing questions posed by Worthington's photographs resonate till today (Rein 1993; Fedorchenko & Wang 2004).

All investigations since Worthington's studies entailed experiments with a freely falling object impacting on the free surface. To gain further insight into such impact

† Present address: Department of Physics and Centre for Fluid Dynamics, The Technical University of Denmark, DK-2800 Kgs. Lyngby, Denmark
‡ Email address for correspondence: d.vandermeer@utwente.nl

events, we built a setup in which we attach the impacting object to a linear motor. In this way we gain full control over the impact velocity, which now turns from a response observable into the key control parameter of the system.

The dynamics of a surface cavity are of enormous practical importance in many natural and industrial processes. Raindrops falling onto the ocean entrain air (Oguz & Prosperetti 1990; Oguz, Prosperetti & Kolaini 1995; Prosperetti & Oguz 1997) and it is this mechanism which is one of the major sinks of carbon dioxide from the atmosphere. Droplet impact and the subsequent void collapse are also a significant source of underwater sound (Prosperetti, Crum & Pumphrey 1989) and a thorough understanding is therefore crucial in sonar research. High-speed-water impacts and underwater cavity formation are moreover of relevance to military operations (Gilbarg & Anderson 1948; Lee, Longoria & Wilson 1997; Duclaux *et al.* 2007; Aristoff & Bush 2009). In the context of industrial applications, drop impact and the subsequent void formation are crucial in pyrometallurgy (Liow *et al.* 1996; Morton, Liow & Rudman 2000), in the food industry, and in the context of ink-jet printing (Le 1998; Chen & Basaran 2002; de Jong *et al.* 2006*a*, *b*). A similar series of events as in water can even be observed when a steel ball impacts on very fine and soft sand (Thoroddsen & Shen 2001; Lohse *et al.* 2004; Royer *et al.* 2005; Caballero *et al.* 2007).

Although in some of the literature the deceleration of the impacting body was minimized by choosing the properties of the body such that the velocity of the impactor remained roughly constant during the time the cavity dynamics were observed (Glasheen & McMahon 1996; Gaudet 1998), the velocity of the body nevertheless remained a response parameter set by the system. Our use of a linear motor to accurately control the position, velocity and acceleration of the impacting object constitutes the key difference between our work (see also Bergmann *et al.* 2006; Gekle *et al.* 2008, 2009) and all previous literature.

In this paper, we will use observations from experiments and boundary integral simulations to construct a model which accurately describes the radial dynamics of the cavity. In § 2 we present results from our controlled experiment and compare them to the boundary integral simulations. More specifically, in § 2.3 we discuss the dynamics of the free surface and continue in § 2.4 with the topology and magnitude of the flow surrounding the cavity obtained by particle image velocimetry (PIV).

In § 3 we will derive a model which captures the radial dynamics of the cavity. We will use the model to investigate the following key characteristics of the transient surface cavity. First, the depth at which the pinch-off will occur is discussed in § 4.1. Second, in § 4.2 the amount of air entrained by the cavity collapse is studied. In both subsections, experiments and simulations are compared to the model results. The paper is concluded in § 5.

2. Experimental and numerical results

2.1. *Experimental setup and procedure*

A sketch of the setup is seen in figure 1(*a*). A steel disk of radius h_0 is mounted on top of a thin rod (∅ 6 mm). The rod runs through a seal in the bottom of a large tank (500 mm × 500 mm × 1000 mm) and is connected at the lower end to a Thrusttube linear motor which is used to determine and control the velocity and acceleration of the disk. The position of the motor (and thus of the disk) along the vertical axis is measured with a spatial accuracy of 5 μm over a range of 1 m, the large acceleration

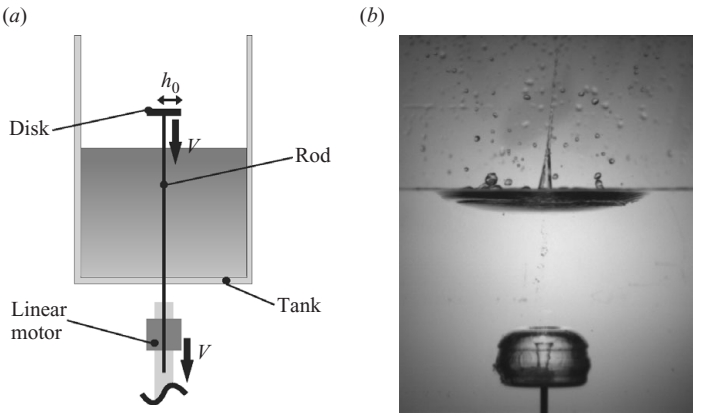

FIGURE 1. (*a*) Schematic illustration of the experimental setup with the linear motor controlling the rod and disk. The vertical rod runs through a seal in the bottom of the glass water tank and is pulled down by the linear motor in order to impact the disk on the water surface. Here, h_0 is the radius and V the controlled and constant velocity of the disk. (*b*) The formation of an upward and downward jet after the cavity has closed. In the present study we will focus on the cavity dynamics until pinch-off, just before the jet formation.

of the motor (up to $30g$, with g the gravitational acceleration) makes it possible to perform impact experiments with constant velocities up to 5 m s^{-1}.

The disk has a thickness of 2.0 mm and its sides are smoothly machined. In all experiments presented in this paper, the water is found to separate at the bottom 90° corner of the disk and not to wet the disk's small vertical sides. The effect of the small diameter of the rod on the global flow and dynamics of the cavity is assumed to be negligible. As the minimum radius for the disk used in the experiments is 10 mm, the ratio of the cross-sectional area of the rod and the surface of the disk is always smaller than 9 %. Since the rod is mounted in the centre of the disk, where stagnation would normally occur, the influence on the radially outward flow below the disk is presumably small.

Using the flat-plate approximation, we can also estimate the direct contribution of the boundary layer of the rod to the axial flow. The boundary layer thickness δ for a flat plate is given by Blasius' solution $\delta \approx 5\sqrt{\nu \Delta t}$, where ν is the kinematic viscosity of water and Δt the time which the boundary layer has to develop. We will equate the time Δt to the duration of the experiment, namely, to the time interval starting from the impact of the disk until the collapse of the void, which in our experiments is found to scale as $\Delta t_{impact} \approx 2.2\sqrt{h_0/g}$, as will be discussed in detail in §4.1. For the largest disk size in the experiment $h_0 = 40$ mm, this result predicts a maximum boundary layer thickness of 1.8 mm. Under most experimental conditions of this study it is considerably thinner.

In our experiments we pull the disk down with a constant velocity V. Making this main control parameter dimensionless, we obtain the Froude number $Fr = V^2/(gh_0)$. The liquid properties are expressed in terms of the Reynolds number $Re = Vh_0/\nu$ and the Weber number $We = \rho V^2 h_0/\sigma$, where σ denotes the surface tension and ρ the fluid density. Since the Reynolds number and the Weber number are large on the scales of our experiment (figure 1), viscosity and surface tension do not seem to play a role. To be more precise, in our experiment the Reynolds number ranges between 500 and 1.6×10^4 and the Weber number ranges between 34 and 8.8×10^3. Note however that under only slightly different conditions, namely, replacing the disk by a

cylinder submerged in water to avoid the splash, capillary waves do play a role (see Gekle *et al.* 2008). For the impact of a disk we find the only important dimensionless parameter to be the Froude number, i.e. the ratio of kinetic to gravitational energy, which ranges from 0.6 to 200 in our experiments. It is convenient to use the amount of time τ remaining until cavity collapse which is given by $\tau = t_{coll} - t$ with t_{coll} the collapse time.

A last consideration is the recirculation time. The impact takes place in a tank of finite size L and one expects that if the recirculation time becomes of the same order as the impact duration, the results will be influenced. The recirculation time can be estimated as the time a fluid particle of velocity V – set into motion by the disk – needs to move to the wall and back to the impact area, i.e. $\Delta t_{circ} \approx 2(L/2)/V$. As mentioned above, the duration of the impact can be estimated as $\Delta t_{impact} \approx 2.2\sqrt{h_0/g}$. The condition $\Delta t_{circ} > \Delta t_{impact}$ now leads to $Fr < (1/2.2)^2(L/h_0)^2 \approx 0.21(L/h_0)^2$. In the worst case, namely when the largest disk ($h_0 = 0.04$ m) is used, this amounts to $Fr < 32$, which is much larger than all experimentally attainable values for this disk size. The same conclusion can be drawn for the other disk sizes from a similar calculation.

The limitations of our experimental setup provide a second reason why recirculation is not a concern: the maximum distance Z the disk can travel at constant velocity in our experiment is smaller than L, as the tank is typically filled to a height of 600 mm ($= 1.2L$), but a considerable distance is needed to decelerate the disk at the employed high impact velocities. This means that there is an experimental upper bound for the duration of the impact set by $\Delta t_{exp} = Z/V < L/V < \Delta t_{circ}$ which confirms that recirculation does not affect our experiment.

2.2. *Numerical method*

The numerical calculations are performed using a boundary integral method (Oguz & Prosperetti 1993; Power & Wrobel 1995; Prosperetti 2002) based on potential flow. This assumption excludes viscous effects and vorticity, which due to the short duration of the phenomenon and the high Reynolds number seems reasonable. The boundary integral formulation would allow for the inclusion of air as a second ideal fluid phase, but as the air creates secondary effects which are not the subject of this study we have opted to leave it out. These secondary effects include the Kelvin–Helmholtz instability in the last stages of the pinch-off (Bergmann *et al.* 2006) and the surface seal at high impact speeds. The surface seal in the experiment is discussed in the next section.

Our code uses an axisymmetric geometry thus reducing the surface integrals to one-dimensional line integrals. For the time-stepping an iterative Crank–Nicholson scheme is employed. The size of each time step is calculated as $t_{step} = f \min(t_{node})$ with $t_{node} = \Delta s / v_{node}$, where Δs is the distance to the neighbouring node and v_{node} the local velocity. With the safety factor f chosen to be 5 % this procedure reliably prevents collisions of two nodes which would lead to serious disturbances in the numerical scheme. The number of nodes is variable in time, with the node density at any particular point on the surface being a function of the local curvature. This procedure guarantees that in regions with large curvatures, especially around the pinch-off point, the node density is always high enough to resolve the local details of the surface shape. At the same time, no computation power is wasted on an exceedingly high node density in flat regions towards infinity (which in our simulations is chosen to be 100 disk radii away from the central axis; note that the bounding container of

the experiments is not included in the simulations.) To avoid numerical disturbances, we employ a regridding scheme in which at every second time step the surface nodes are completely redistributed placing the new nodes exactly half-way between the old nodes.

A particularly sensitive issue is the modelling of the crown-shaped splash created when the disk impacts the water surface. After first shooting upwards in a ring shape, the splash quickly breaks up into a large number of drops (which are ring shaped due to the imposed axial symmetry). These drops do not further influence the cavity behaviour and therefore need not be accounted for in our numerical code. In most simulations presented in this work, the crown-shaped splash evolves normally until drop pinch-off. As this happens, the surface is reconnected at the pinch-off location and the drop is discarded.

2.3. *Interface*

The series of events typical for the experimental range of $1 < Fr < 100$ is seen in the snapshots of figures 2(*a*), 2(*b*) and 2(*c*). Upon impact, an outward moving crown of water (the splash) is formed. A void is created which collapses due to the hydrostatic pressure and a singularity arises when the collapsing walls of the void collide with each other. Two jets emerge in this experiment: one upwards straight into the air, and one downwards into the entrained air bubble (see figure 1*b*).

In each of figures 2(*a*), 2(*b*) and 2(*c*) the experimental sequence is overlaid with the results of our boundary integral simulation. For $Fr = 0.85$ and $Fr = 3.4$ (figures 2*a* and 2*b*), the cavity dynamics is found to be captured extremely well by the numerical result, represented by the overlaid lines. Note that this is a one-to-one comparison between simulation and experiment, without any rescaling in time or space. Due to the axisymmetry of the code it is not possible to capture the full details of the splash, and since our focus is on the cavity dynamics we chose to simply take out any droplet which is released from the splash in the simulations. Surface tension however still expresses itself in small capillary waves in the region of the splash. These waves are most notable in figure 2(*a*). As was mentioned before, similar capillary waves (but from a different origin) are found to have a significant influence on the closure of the cavity for a submerging cylinder (Gekle *et al.* 2008). For the impacting disk discussed in this paper however they do not affect the closure.

The results for $Fr = 0.85$ in figure 2(*a*) illustrate the effect of the relative importance of gravity. In the last frame of figure 2(*a*) it can be seen that the cavity is less symmetric in the axial direction around the closure point compared to the experiment performed at $Fr = 3.4$ shown in figure 2(*b*). In the third sequence at $Fr = 13.6$ (figure 2*c*), which goes beyond the experimental Froude number range described in Bergmann *et al.* (2006), significant deviations between the experimental and the numerical cavity shape are found, most notably in the enlargement of figure 3 at the depth of the cavity closure. The closure of the cavity is found to be somewhat deeper in the numerics as compared to the experiments. This deviation can be attributed to a secondary effect due to the surrounding air, called the *surface seal* (see figure 4). This phenomenon was first reported by Worthington (1908) and later investigated in more detail by Gilbarg & Anderson (1948). Note that the impact experiment of figure 4 is performed under the same conditions as depicted in figure 2(*c*). The cause for the surface seal is the air which flows into the expanding cavity and influences the splash. If the airflow is strong enough the initially outward moving splash will be sucked in towards the

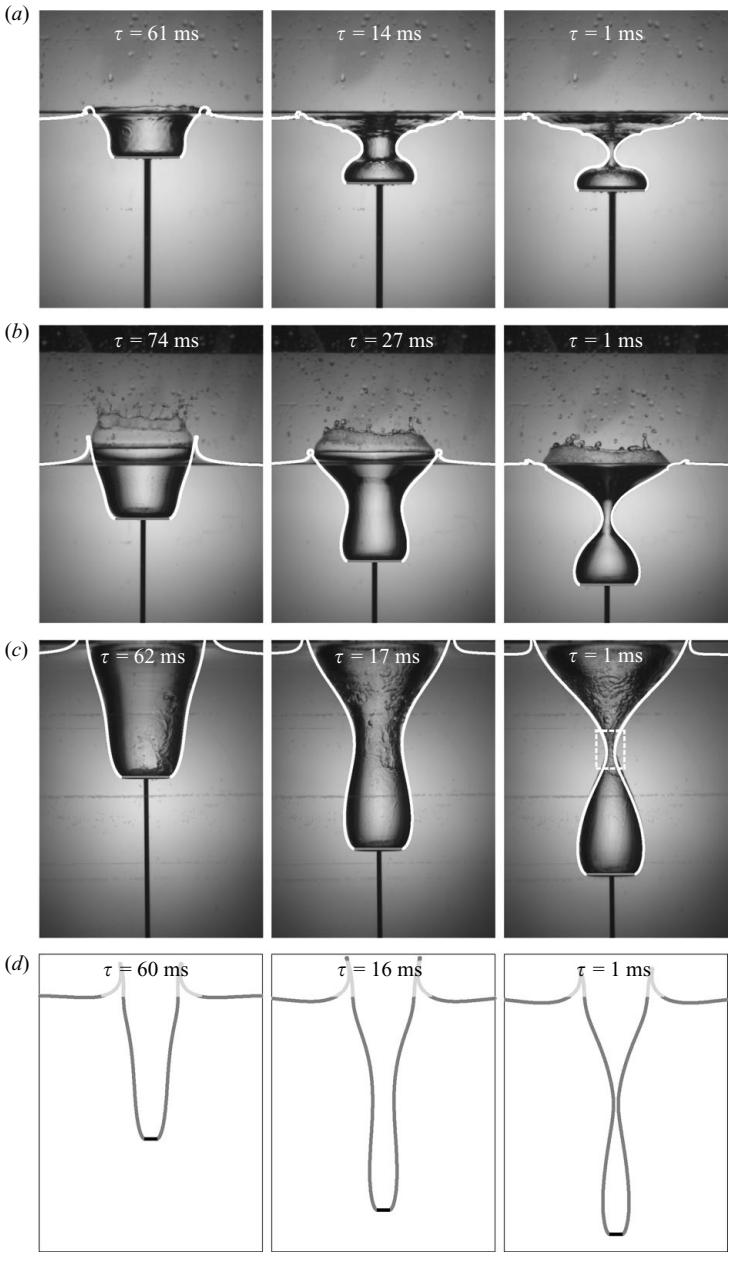

FIGURE 2. Snapshots of the formation and collapse of a surface void in the plunger experiment. A linear motor pulls down a disk of radius $h_0 = 30$ mm through the water surface at a constant velocity. (*a*) For $V = 0.5$ m s^{-1}, i.e. $Fr = 0.85$. The total duration Δt of the experiment is 129 ms from the moment of impact to the pinch-off; (*b*) for $V = 1.0$ m s^{-1} ($Fr = 3.4$, $\Delta t = 133$ ms); (*c*) for $V = 2.0$ m s^{-1} ($Fr = 13.6$, $\Delta t = 137$ ms) and (*d*) for $Fr = 200$ ($\Delta t = 148$ ms). The collapse of the void is imaged at 1000 frames s^{-1}. The lines (overlay) are the void profiles obtained from boundary integral simulations. Without the use of any free parameter, neither in time nor in space, an excellent agreement between the simulation and experiment is found in (*a*) and (*b*). Due to a (mild) surface seal there is a discrepancy between the simulations and the experiment in sequence (*c*), both in the top region near the splash and in the pinch-off region. The region of the dashed box is shown enlarged in figure 3. The conditions of (*d*) are outside the experimental range due to the combination of the limited size of the tank and finite deceleration of the linear motor.

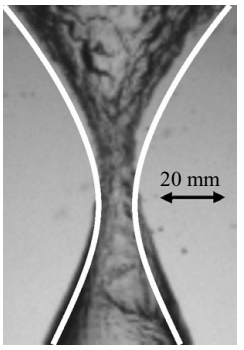

FIGURE 3. Enlargement of the region around the pinch-off point at $\tau = 1$ ms from the sequence (figure 2*c*) ($Fr = 13.6$). A significant discrepancy can be seen for the depth of the pinch-off between the boundary integral simulation (white line) and the experimental recording. The origin of this discrepancy is the airflow in the cavity as will be elaborated elsewhere.

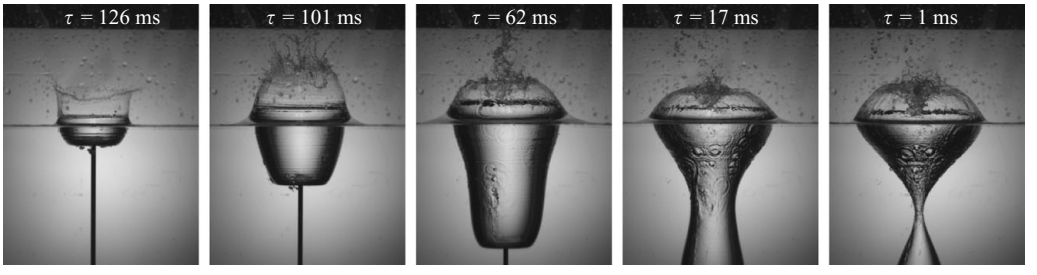

FIGURE 4. Snapshots of the surface seal which occurs for a disk of radius $h_0 = 30$ mm impacting the water surface at a constant velocity of $V = 2.0$ m s^{-1} ($Fr = 13.6$), i.e. under the same conditions as figure 2(*c*).

axis of symmetry and eventually completely seal off the top of the cavity at the undisturbed water surface level.

The surface seal is found to become more pronounced at higher impact velocity, where it occurs earlier and more liquid is involved in the closure. Accordingly, there is also a larger influence on the shape of the cavity at higher impact velocity. Since this paper aims to treat the purely pressure-driven collapse of the cavity, without the contributions of the surrounding air, our experimental range is limited by the occurrence of the surface seal. In the simulations we therefore intentionally do not include the air. This explains the discrepancy of figure 2(*c*) (enlarged in figure 3), since contrary to the experiments, no surface seal occurs in the numerics due to the absence of air. In figure 2(*d*) we go far beyond the experimentally available range by performing simulations at a Froude number of 200.

It is instructive to compare the present boundary integral simulation results with those reported by Gaudet (1998), who reported a bulging contraction of the cavity at the surface level. He found this contraction to close for $Fr \geqslant 200$ and interpreted it as a surface seal in the absence of air. We found no evidence for such a surface seal in our simulations, even for considerably larger Froude numbers, and surmise that the effect reported by Gaudet (1998) may be connected to using an insufficient number of nodes in the splash region caused by the limited amount of computational power available at that time.

2.4. *Flow field*

In the previous subsection we found the experimental shape of the impact cavity to be well described by our boundary integral simulations if no surface seal occurs. The question we will address in this subsection is whether the simulations also give an accurate description of the surrounding flow field. To this end we will measure the velocity field around the transient cavity through high-speed PIV. These experiments are crucial to check the validity of the boundary integral simulations, as the presence of a solid boundary, namely the impacting object, will induce vorticity in the flow. We will compare the experimental flow field to the boundary integral results and finally investigate the radial flow at the depth of closure in more detail.

To perform the PIV measurements, the fluid is seeded with small DANTEC Dynamics polyamid tracer particles of radius 25 μm and density 1030 kg m^{-3} which follow the flow. A laser sheet shines from the side through the fluid, creating an illuminated plane through the symmetry axis of the cavity. The light scattered by the particles is captured by a high-speed camera at a frame rate of 6000 frames s^{-1} and a resolution of 1024×512 pixels. The series of recorded images is then correlated by multipass algorithms, using DaVis PIV software by LaVision, in order to determine the flow field in a plane in the liquid. The correlation was performed in two passes at subpixel accuracy, using 64×64 pixels and 32×32 pixels interrogation windows. The windows overlap by 50 %, resulting in one velocity vector every 16×16 pixels.

In order to obtain high-resolution PIV measurements of the flow around the cavity, we made use of the reproducibility of the experiment. The left side of each of the images of figure 5 shows the flow around the expanding void by combining the results of four separate PIV measurements at different depths. In this fashion PIV experiments were performed for a field of view of 96 mm $\times$ 56 mm at a spatial resolution of 0.9 mm (in figure 5 only 0.7 % of the measured vector field is shown). This high resolution makes it possible to simultaneously compare the global flow, as well as the smaller flow structures at the pinch-off depth and the disk's edge.

The right side of each image of figure 5 shows the numerically obtained cavity profile and flow field. In figure 6 one of them, namely figure 5(*c*), is shown for more detailed comparison. At first sight there appears to be a good agreement, but one would like to obtain a more quantitative comparison between experiment and simulation. This is provided in figure 7, which shows contour plots of the axial flow component (figure 7*a–d*) and the radial flow component (figure 7*e,f*) obtained from the PIV measurements (at the left side of each image) and boundary integral simulations (at the right side of each image). From this figure it is clear that the magnitude as well as the topology of the flow are in excellent agreement. Figures 5 and 7 are a one-to-one comparison between simulation and experiment, and we stress once more, without the use of any free parameter.

In addition to the above, the experimental pictures of figure 7 reveal that our initial assumption to neglect the influence of the rod on the flow (see § 2) is correct. The rod itself is clearly visible in the experimental snapshot of figure 5(*a*) and the PIV software has correctly detected its downward movement, as can be seen in figure 7(*a, b*). From the same figures we also conclude that outside a thin region around the rod the flow remains unchanged. Most importantly, the outward flow at the edges of the disk in figure 7(*e*), which is responsible for the expansion of the void, is unaffected by the presence of the rod. This can be understood from the fact that below the disk the radial flow component decays quickly towards the centre of the disk whereas the vertical component in the centre is equal to the disk speed. As the fluid in the central region hardly moves with respect to the disk, the presence of the rod has a negligible

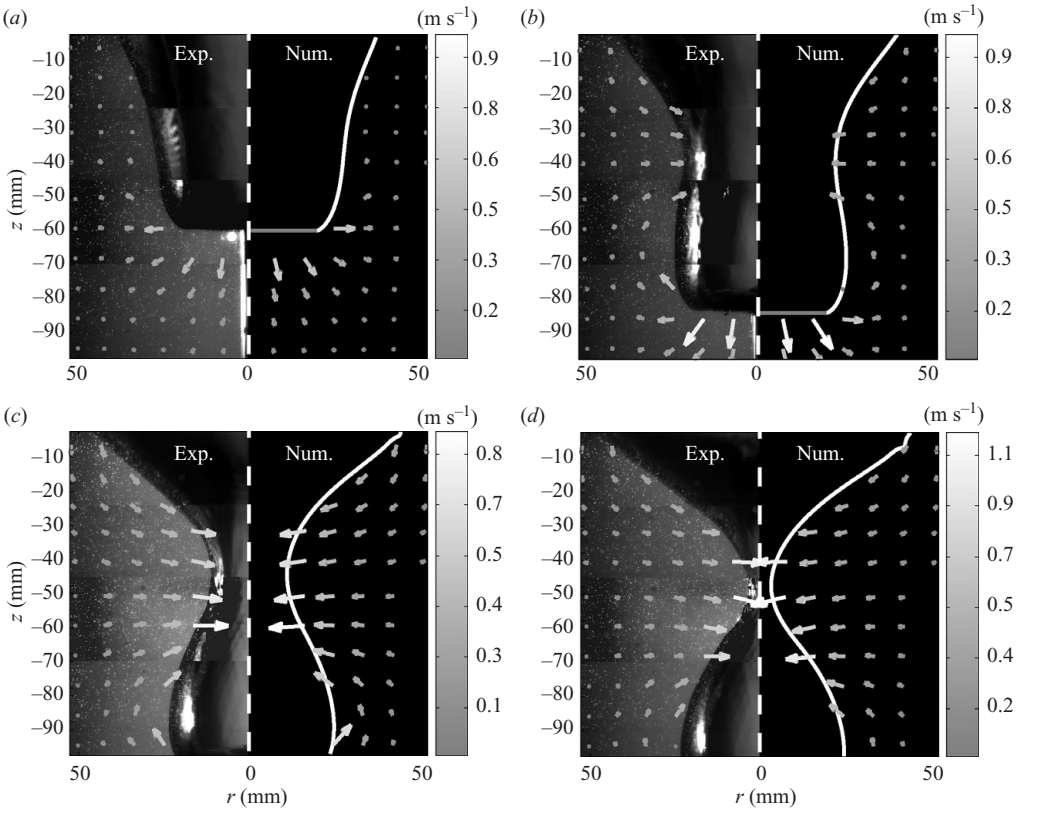

FIGURE 5. Comparison of the flow field obtained from experiments and boundary integral simulations for a disk of radius $h_{disk} = 20$ mm which impacts with a velocity of $V = 1.0$ m s^{-1} ($Fr = 5.1$). The figures show the flow field at $\tau =$ (*a*) 49 ms; (*b*) 25 ms; (*c*) 7 ms and (*d*) 1 ms. (The elapsed time from the moment of impact is given by $t =$ (*a*) 60 ms, (*b*) 84 ms, (*c*) 102 ms and (*d*) 108 ms, respectively.) The left side of each image shows the flow field (overlaid vectors) obtained from the experiment by four high-speed PIV recordings at 6000 frames s^{-1}. The four separate recordings were taken at different depths and combined to give the flow field at high resolution. The recordings on the left side of each image also illustrate the degree of reproducibility of the experiment, as the match between the four PIV recordings at different depths obtained from four repetitions of the same experiment is perfect. For clarity only 0.7 % of the measured vectors is shown. The right side of each of the images shows the void profile and the corresponding flow field (overlaid vectors) obtained from the boundary integral calculations.

effect on the flow field. We conclude that the boundary layer of the rod makes no contribution whatsoever to the flow field around the cavity.

This is confirmed by computing the azimuthal vorticity from the experimental data (not shown). Non-zero vorticity is confined to a small region along the rod and near the edge of the disk. The amount of vorticity in the bulk of the fluid fluctuates randomly around zero and its magnitude falls within the measurement error everywhere, except for the regions mentioned above. In addition we can conclude that, in spite of the large Reynolds numbers present in the flow, turbulence does not play a role. This can be traced back to the short duration of the impact event which does not allow for turbulent structures to develop.

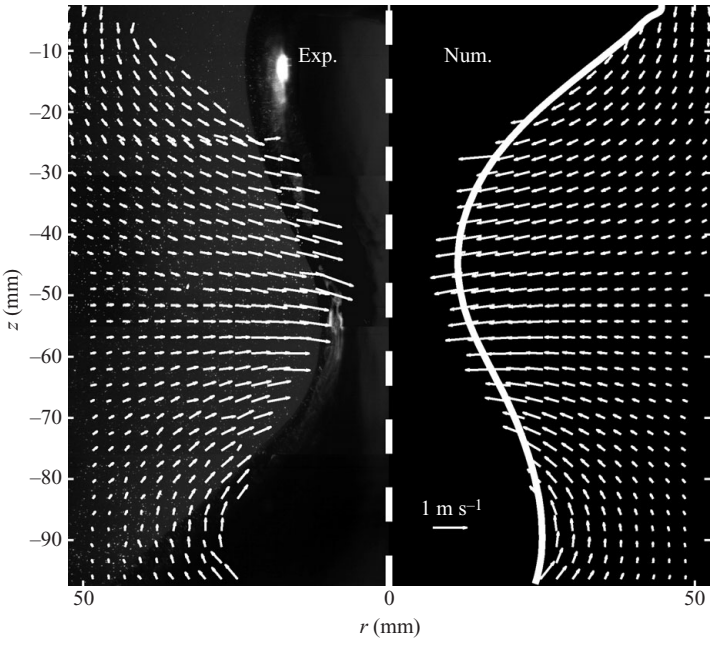

FIGURE 6. The detailed flow field of figure 5(*c*) with every third vector in each of the two directions shown, i.e. about 11 % of the measured vectors.

In figure 8 the experimental flow at the closure depth is compared with numerics up to seven disk radii in radial direction in order to obtain a more quantitative measure of the magnitude of the deviations between the numerical and experimental flow field. We find this deviation to be typically of the order of 0.01 m s^{-1}, but it can be slightly larger if the flow velocity is small. In the region close to the free surface the small deviations in the radial flow may be caused by its unsteady and nonlinear nature as is discussed by Thoroddsen, Etoh & Takehara (2007). The larger inaccuracy at low flow velocities in both components is generic to the PIV method and can most clearly be seen to occur for $\tau = 10.5$ ms in figure 8(*b*). Overall, a very good agreement is found between the far field flow in the numerics and experiments.

Both in the experiment and simulation we observe that during the expansion of the void the magnitude of the outward radial flow falls off with the distance to the symmetry axis (figure 8*a*). However, once the cavity starts to collapse inward there will be a region around the cavity where the (radial) direction of the flow is reversed and there will be an axisymmetric curved plane (manifold) where the radial flow component vanishes. Here this happens between $\tau = 30.5$ and $\tau = 20.5$ ms (cf. figure 8*a*). In § 3.2 we will discuss in detail how this reversal of the radial flow expresses itself in the radial dynamics of the cavity.

3. Modelling the cavity dynamics

In this section we will first derive a simple analytical model for the radial dynamics of the transient cavity. Secondly, we will investigate the surrounding flow, which enters the model through two of the free parameters and causes an asymmetry of the collapse. In the last part of this section we compare the model to the radial dynamics of the cavity observed in experiment and simulation.

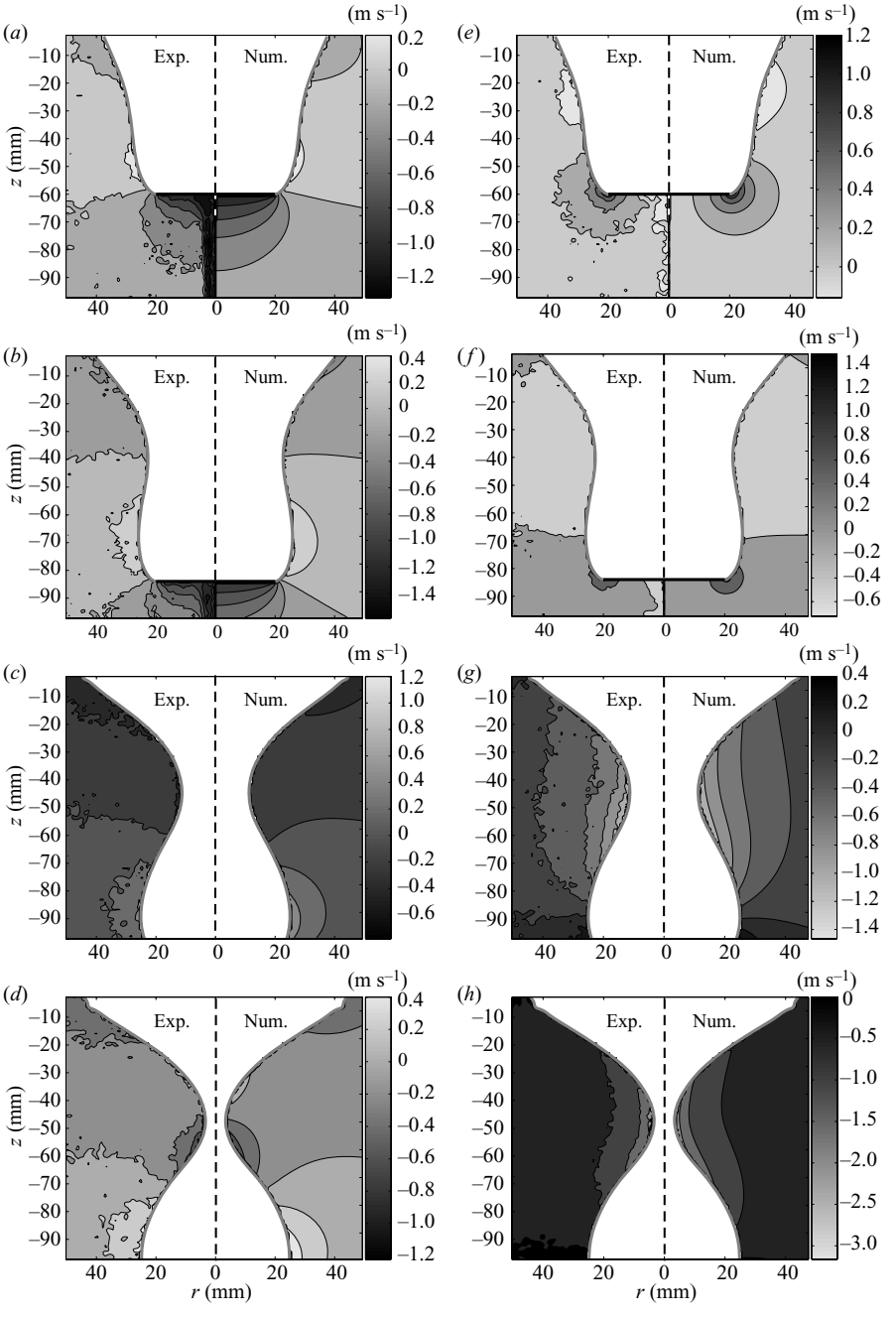

FIGURE 7. The axial (*a–d*) and radial (*e–h*) components of the flow field representing the same velocity data as in figure 5 and taken at the same times $\tau = 49$ ms (*a,e*), 25 ms (*b,f*), 7 ms (*c,g*) and 1 ms (*d,h*). (The elapsed time from the moment of impact is given by $t = 60$ ms (*a,e*), 84 ms (*b,f*), 102 ms (*c,g*) and 108 ms (*d,h*), respectively.) (*a–d*) Compare a contour plot of the axial flow component from the experiment (left side of each image) with that of the numerics (right side of each image). (*e–h*) Show a similar comparison in a contour plot of the radial flow component from the experiment (left side of each image) and numerics (right side of each image). Apart from the region where the rod is pulling down the disk in the experiment, which is absent in the simulation, both components of the flow field show excellent agreement between the experiments and numerical calculations.

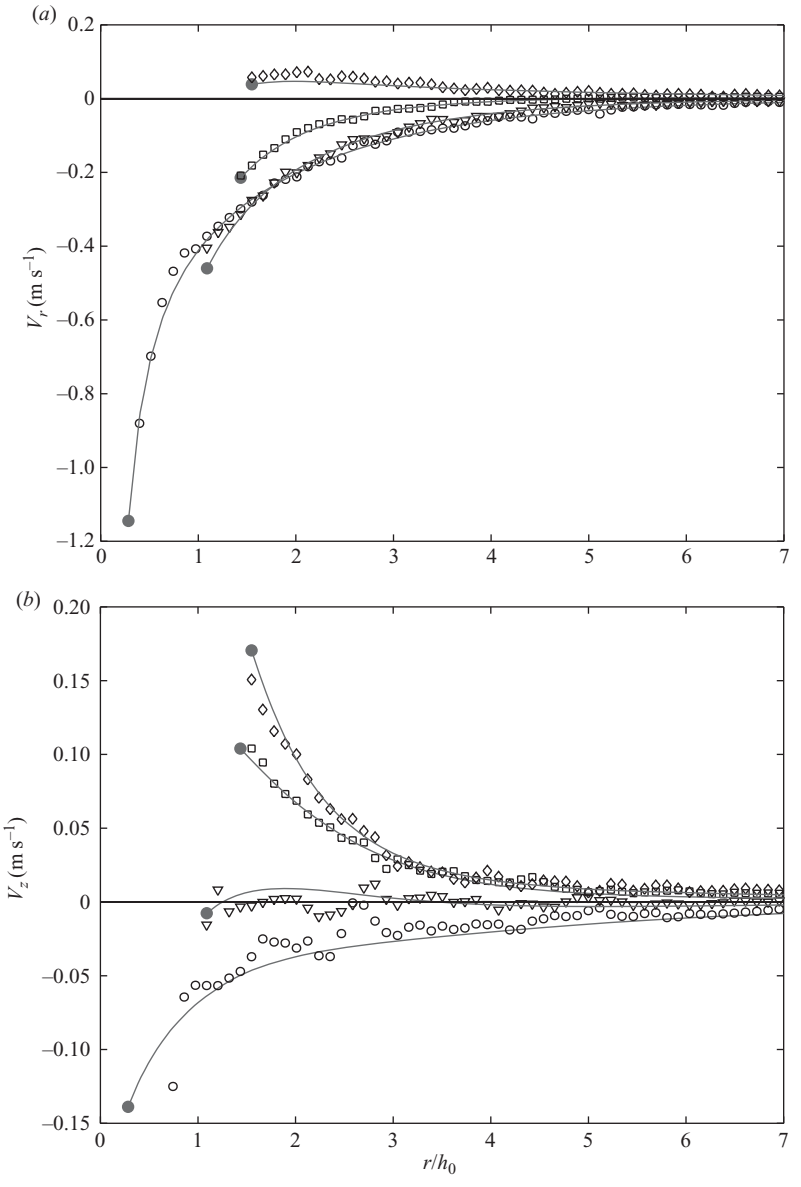

FIGURE 8. Radial (a) and axial (b) components of the flow at the depth of closure z_{coll} for a disk of radius $h_{disk} = 10$ mm which impacts at a velocity of $V = 1.0$ m s^{-1} ($Fr = 10.2$). The symbols show the result obtained from the PIV measurements at different times, $\diamond$: $\tau = 30.5$ ms; $\square$: $\tau = 20.5$ ms; ∇: $\tau = 10.5$ ms and $\circ$: $\tau = 0.5$ ms, and the lines are the corresponding numerical results from the BI simulation. Note that these lines end on the cavity surface (solid dots). The PIV data is an average of six subsequent measurements obtained from the high-speed PIV recordings at 6000 frames s^{-1}. In consequence, the v_r and v_z velocity components shown here are the average over 1 ms.

3.1. *A model for the radial cavity dynamics*

The full analytical modelling of a cylindrical symmetric collapse of the transient cavity presents the difficulty of a coupling between the free surface and the flow surrounding the cavity. To tackle this difficulty we propose the convenient simplification of dividing

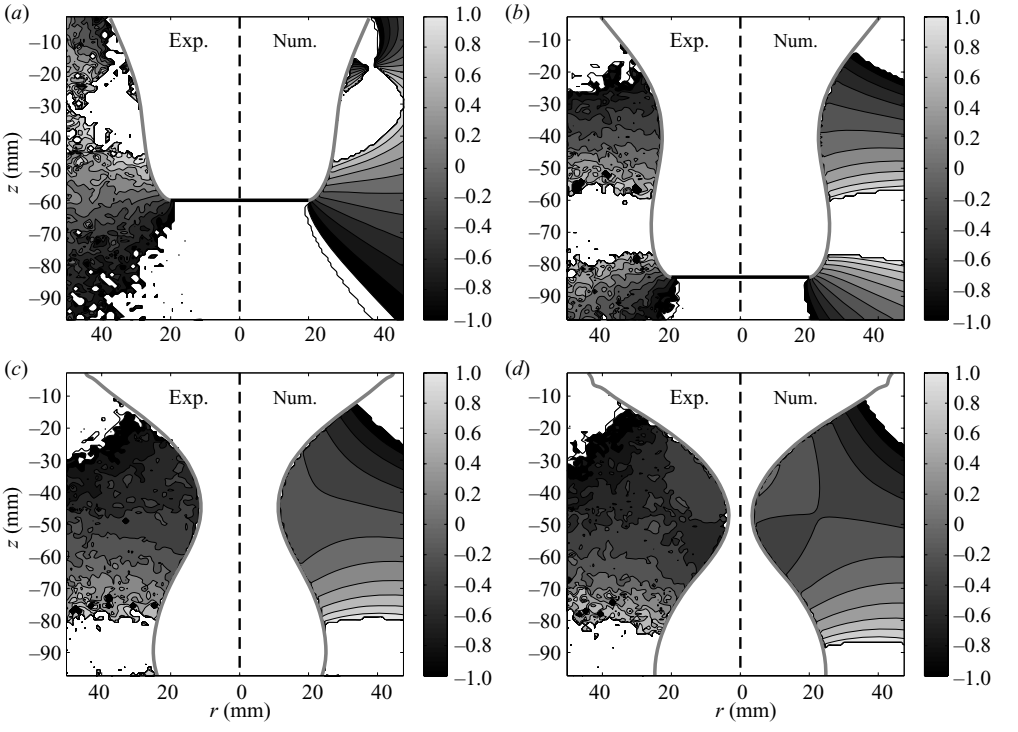

FIGURE 9. The absolute value $|v_z/v_r|$ of the ratio of the axial and radial components of the flow field, from the same velocity data as in figure 5 and taken at the same times $\tau = (a)$ 49 ms, (b) 25 ms, (c) 7 ms and (d) 1 ms. (The elapsed time from the moment of impact is given by $t = (a)$ 60 ms, (b) 84 ms, (c) 102 ms and (d) 108 ms, respectively.) The region around the minimal neck radius for which $|v_z/v_r| \ll 1$ grows as the pinch-off is approached, but it is clear that this assumption is not valid along the whole cavity profile. The regions outside the cavity without any filling (the larger white areas) indicate that $|v_z/v_r| > 1$.

the problem into a set of quasi two-dimensional problems. If the axial component of the flow is small compared to the horizontal flow components, we can approximate the flow as to be confined to the horizontal plane. In this way an equation for the collapse of a two-dimensional bubble will suffice to describe the cavity dynamics at an arbitrary depth.

Figure 9 shows the validity of the assumption $v_z/v_r \ll 1$ along the cavity profile. In the early stages (figure 9*a*) this condition is not fulfilled and at the maximum cavity radius this assumption will always be violated, since the radial flow vanishes here by definition. However, as the cavity collapses the radial flow increases and there is a rapidly growing region around the minimal radius in which $v_z/v_r \ll 1$.

To derive the equation for the collapse of a two-dimensional bubble we will closely follow a derivation given in Oguz & Prosperetti (1993) and Lohse *et al.* (2004). The argument starts by writing the Euler equation in cylindrical coordinates, and neglecting the vertical flow component and its derivatives. This means that we assume the flow to be quasi-two-dimensional at any depth along the cavity. The azimuthal components can be ignored due to the axial symmetry, leaving the following equation:

$$\frac{\partial v_r}{\partial t} + v_r \frac{\partial v_r}{\partial r} = -\frac{1}{\rho}\frac{\partial p}{\partial r}\,, \tag{3.1}$$

where ρ denotes the density of the liquid. Under the above assumption of negligible v_z and thus $\partial v_z/\partial z$, the continuity equation and the boundary conditions on the surface of the void lead to a second equation

$$r v_r(r, t) = h(t)\dot{h}(t). \tag{3.2}$$

Here, $h(t)$ is the radius of the cavity and its derivative $\dot{h}(t)$ the velocity of the cavity wall at any depth z below the surface. Substituting (3.2) into (3.1) gives

$$\frac{\partial}{\partial t}\left(\frac{h\dot{h}}{r}\right) + \frac{\partial}{\partial r}\left(\frac{1}{2}v_r^2 + \frac{p}{\rho}\right) = 0. \tag{3.3}$$

We can integrate this equation over r from the cavity wall h to a reference point h_∞, where the flow is taken to be quiescent. This integration yields a Rayleigh-like equation for the void radius at a fixed depth z,

$$\left[\frac{\mathrm{d}(h\dot{h})}{\mathrm{d}t}\right]\log\frac{h}{h_\infty} + \frac{1}{2}\dot{h}^2 = gz. \tag{3.4}$$

Here, we have used the fact that the pressure (p_∞) driving the collapse of the cavity is provided by the hydrostatic pressure $\rho g z$, where z denotes the depth below the fluid surface. Close to the collapse, the quantity h_∞ can be interpreted as the length scale related to the matching of an inner and outer flow regions. In the (inner) region near the neck the induced flow looks like a collapsing cylinder as described by (3.4), whereas in the (outer) region far from the neck, the flow resembles that of a dipole (plus its image in the free surface). A complete description of the flow would require the matching of these two regions, where h_∞ would be determined in the process as the cross-over length scale. h_∞ would thus be expected to be of the order of a typical length scale of the process, such as the distance of the cavity surface to the plane where the radial flow vanishes (see figure 8*a*). Therefore, strictly speaking, h_∞ is a function of the Froude number, the depth z and time. In the model presented below we follow a different simplified route and for every Froude number set h_∞ to a constant value (a time-averaged value of its dynamics). This value then depends on depth only through its Froude number dependence.

Note that the marked dependence on h_∞ for this two-dimensional collapse is due to the presence of the logarithmic term in (3.4). In the corresponding three-dimensional problem of the bubble collapse the flow field vanishes much faster as $1/h^2$ and the dependence on h_∞ can in most cases be neglected.

We will now use (3.4) to analyse the radial dynamics from the initial impact of the disk t_0 to the time of closure of the cavity t_{coll} at arbitrary depth z. In order to obtain an analytical approximate solution, we decompose the cavity dynamics into three different stages, depicted schematically in figure 10. In this figure the time intervals corresponding to the different stages are denoted as Δt_{expa}, Δt_{ctra} and Δt_{coll}, respectively. In the first two stages, during Δt_{expa} and Δt_{ctra}, the dynamics is dominated by the hydrostatic pressure forcing and inertia. In these stages we observe that the water is first pushed aside by the passing disk, creating an expanding void. At the maximum radius h_{max}, the expansion is halted and the void starts to contract. h_{max} is typically of the order of h_0, e.g. for $Fr = 3.4$ and $Fr = 200$ we find, respectively, $h_{max} \approx 1.3h_0$ and $h_{max} \approx 2.4h_0$. Since $\dot{h}(t_{max}) = 0$, we can assume that $\dot{h}(t)$ is small during this expansion and contraction and we can neglect the second term of (3.4)

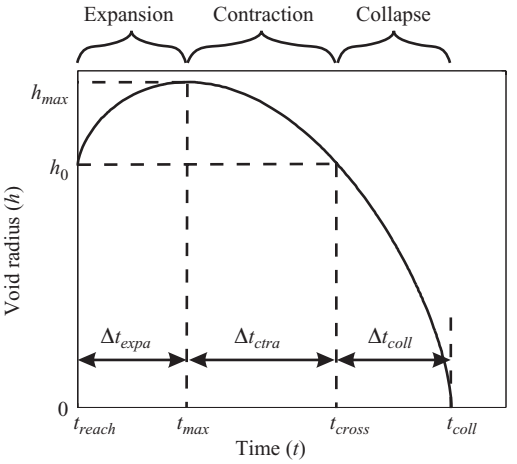

FIGURE 10. Schematic representation of the three stages in the radial dynamics of the cavity at a constant depth z. The first two stages (corresponding to the time interval $\Delta t_{expa} + \Delta t_{ctra}$) are governed by a forcing of the flow by hydrostatic pressure. We can distinguish an expansion and a contraction phase for which the model parameter h_∞ differs considerably. In the third stage (corresponding to Δt_{coll}) the collapsing void accelerates towards the singularity (pinch-off) in which inertia takes over as the driving factor.

leading to

$$\left[\frac{\mathrm{d}(h\dot{h})}{\mathrm{d}t}\right] \log\frac{h}{h_\infty} = gz. \tag{3.5}$$

Since $\log(h/h_\infty)$ varies very slowly in the first regimes, we equate $\log(h/h_\infty) \approx \log(h(t_{max})/h_\infty)$ and we solve (3.5) using $h(t_{max}) = h_{max}$ and $\dot{h}(t_{max}) = 0$, leading to a parabolic approximation for h^2,

$$h^2(z,t) = h_{max}^2 - \frac{gz}{\beta}(t - t_{max})^2\,, \tag{3.6}$$

with $\beta \equiv -\log(h_{max}/h_\infty)$. The above equation holds for both the expansion stage, the time it takes for the void to grow from h_0 to h_{max}, and the contraction stage, the time it takes to shrink back to h_0.

In the third stage, during Δt_{coll}, the collapsing void accelerates towards the singularity and inertia takes over as the only dominant factor driving the dynamics of the cavity. This stage can be described using a different approximation to (3.4). Near the collapse, h approaches zero, h_∞ is typically very large and thus the logarithm diverges. The only way (3.4) can remain valid is when the prefactor of the logarithm vanishes. This means that

$$\frac{\mathrm{d}(h\dot{h})}{\mathrm{d}t} = \frac{1}{2}\frac{\mathrm{d}^2(h^2)}{\mathrm{d}t^2} = 0. \tag{3.7}$$

Integration gives the power law of the two-dimensional Rayleigh collapse (cf. Bergmann *et al.* 2006)

$$h(t) = \sqrt{C}(t_{coll} - t)^{1/2}. \tag{3.8}$$

In § 3.3 the integration constant $\sqrt{C}$ will be determined from continuity of h and $\dot{h}$.

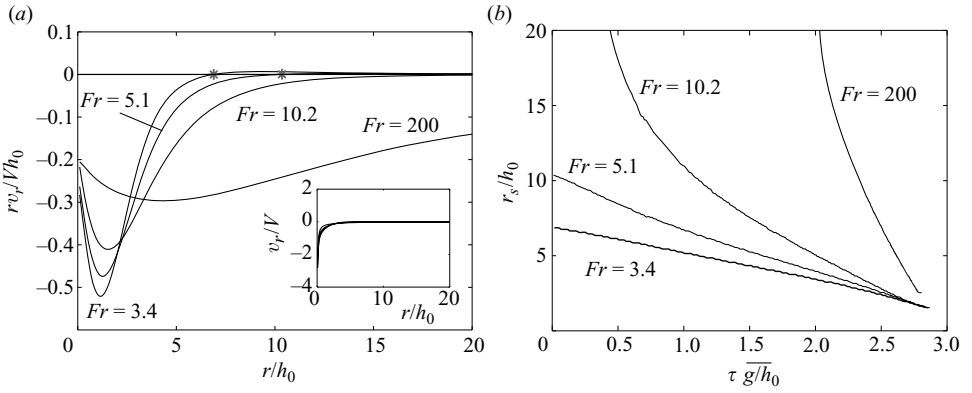

FIGURE 11. (*a*) The radial velocity component v_r at depth of closure just prior to pinch-off (when $h = 0.05h_0$) multiplied by the radial distance r as a function of the same radial distance for different Froude numbers. At the free surface the radial flow is equal to the wall velocity (the last data point shown however is $h = 0.1h_0$ and does not reach this limit.) The distance r_s where the radial velocity is zero and the flow is stagnant in radial direction is indicated by the stars (*). The flow can be seen to resemble a radial sink flow more with increasing Froude number as the minimum of $v_r r$ decreases with increasing Froude number. The inset contains the radial flow velocity v_r itself, to illustrate the increase of v_r as $r \to 0$. (*b*) The distance of the point where the radial flow reverses sign to the symmetry axis, determined at the depth of closure as a function of the normalized time remaining till closure $\tau = t_{coll} - t$. Below the curves the flow is directed inwards, above them it is directed outwards. The radial distances of the flow reversal point at $\tau = 0$ in this figure correspond to the stars (*). The distance of the point of flow reversal is related to the length scales h_∞^{ctra} and h_∞^{expa}, which are therefore expected to behave similarly in time.

3.2. *The influence of the flow on* h_∞

As an intermezzo in the exposition of the model we now turn to an important point, namely, that there is a significantly different quality to the flow in the expansion and the contraction stages. Figure 11 shows clearly what was hinted at in our discussion of figure 8, namely, that in the expansion phase the outward radial flow simply decays with the radial distance, whereas in the contraction phase the radial flow changes sign at finite distance from the free surface. This is due to the fact that the fluid flows outward until the cavity reaches its maximum radius h_{max}, from where it will start to move inward, creating a reversed-flow region around the cavity wall which grows in time. Although in both stages hydrostatic pressure is the dominant factor driving the dynamics of the cavity, there is this dissimilarity in the surrounding flow which needs to be incorporated into the model. To investigate the dynamics of this dissimilarity in detail, we turn to the simulations from which we can obtain the flow field (used in figures 11 and 12) with an arbitrarily fine resolution.

Figure 11(*a*) shows the radial flow component v_r multiplied by the radial distance r to the axis of symmetry at the depth of pinch-off just prior to the moment at which the cavity pinches (when $h = 0.05h_0$). On the free surface the radial flow is equal to the wall velocity, $v_r(r = h) = \dot{h}$, and locally it resembles a two-dimensional sink, the strength of which falls off as $1/r$. Therefore, if we multiply v_r with r we eliminate the geometrical contribution to the flow. For the lower Froude numbers of 3.4 and 5.1 the radial flow component reverses direction at closure depth and time at some distance r_s (stars). At the higher Froude numbers (10.2 and 200) no such point is observed within the numerical domain, which extends to 100 disk radii in the radial direction.

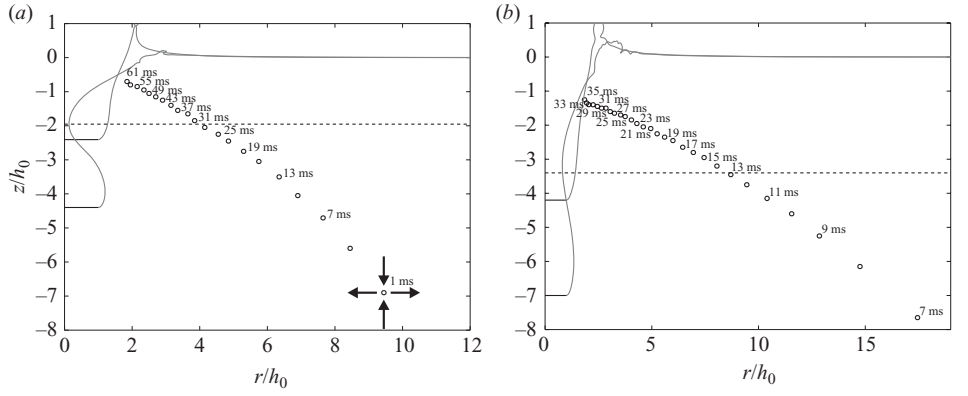

FIGURE 12. The open circles show the path of the stagnation point of the flow for (*a*) $Fr = 3.4$ and (*b*) $Fr = 10.2$. For (*a*) the first observation of the stagnation point is made at $\tau = 61$ ms until 1 ms before closure at intervals of 3 ms. In (*b*) the first observation is made at $\tau = 35$ ms until 7 ms before closure at intervals of 1 ms. For clarity the time till closure is indicated only for every second observation. The arrows in (*a*) illustrate the direction of the local flow around the stagnation points in (*a*) and (*b*). Further more, the void profiles at the time of the first and the last observations are shown. The depth of closure is indicated by the horizontal dashed line.

This does not mean that such a flow reversal point is absent during the complete time of the collapse, as can be seen in figure 11(*b*) where we plot the location of the flow reversal point as a function of time. The radial flow reversal point comes into existence at the wall of the void at the moment that the expanded cavity starts to collapse and the flow direction is reversed inward. From then onwards, this point travels away from the axis of symmetry as the collapse is approached ($\tau \to 0$). In the same figure we also observe that for a higher Froude number the radial flow reversal point travels outward much faster during the cavity collapse as compared to the low *Fr* case.

The position of the radial flow reversal point at different depths describes a curve in the (r,z)-plane. Similarly, there is a curve at which the axial flow component changes sign, as water flows in from above and below while the cavity collapses. These flow-reversal curves can be characterized by a stagnation point (or saddle point) in the (r,z)-plane, which is the point where the two curves intersect and both the axial and the radial velocity components change sign. This stagnation point corresponds to a circle around the cavity in three dimensions. In figure 12 the path of this stagnation point is shown for (*a*) $Fr = 3.4$ and (*b*) $Fr = 10.2$. For both simulations the stagnation point not only moves away from the axis of symmetry as the pinch-off is approached, but it is also seen to move down in the axial direction and at some point even to cross the depth of closure. A similar path of the stagnation point is observed for all the simulations of figure 11 and only at one instant during the collapse of the cavity does the radial flow reversal point at closure depth truly coincide with the stagnation point.

The above leads us to three observations which are relevant for our model of the cavity collapse. (i) Since radial flow reversal at closure depth occurs when the cavity starts to collapse, the character of the flow differs between the expansion and the contraction stages. Since h_∞ is the radial distance at which the flow can be assumed to be quiescent ($\boldsymbol{v} = 0$ and $p = p_\infty = \rho g z$) it is related to the structure of the surrounding flow, and it is therefore justified to assume different values of h_∞ in the respective

stages. We will take $h_\infty \equiv h_\infty^{expa}$ in the expansion stage and $h_\infty \equiv h_\infty^{ctra}$ in the contraction stage of the model. Just like h_∞ in § 3.1, h_∞^{expa} and h_∞^{ctra} are set to a constant value, representing the time-averaged behaviour of h_∞ in each respective stage. The two constants h_∞^{expa} and h_∞^{ctra} can be identified as the time average of a function $h_\infty(t)$ expressing the motion of the stagnation point in the flow which is continuously moving outward during the contraction stage, leading to a markedly different value of the constants in the two stages. (ii) As the distance of the radial flow reversal during the contraction moves away faster at higher Froude number, presumably a higher value for h_∞^{ctra} needs to be taken for larger Froude numbers. (iii) In Bergmann *et al.* (2006) we found that there are two scaling regimes for the neck radius, the first regime where the neck radius scales as a pure power law of time (as in (3.8)), and the second regime, where a logarithmic correction of time has to be taken into account. The cross-over between the two regimes is given by the length scale $h_{max}^2/h_\infty^{ctra}$. As we find from figure 11(*b*), for all Froude numbers the distance of the radial flow reversal increases as the pinch-off is approached. Although in theory we assume h_∞^{ctra} to be constant, in reality h_∞^{ctra} thus increases as the pinch-off is approached. This means the cross-over length scale $h_{max}^2/h_\infty^{ctra}$ decreases with time.

Therefore the time needed for the collapsing neck to decrease to $h_{max}^2/h_\infty^{ctra}$ will be longer as compared to the assumption of a constant (initial) value for h_∞^{ctra} and may even never reach this second regime. The effect is stronger for increasing Froude number, since the radial flow reversal point at closure depth moves away faster and further at higher Froude number.

3.3. *The free parameters of the model*

In this section, we continue our derivation of a simplified model for the radial cavity dynamics started in § 3.1. As argued in the previous subsection it is justified to assume different (constant) values for h_∞ during the expansion and contraction stages of the void. We therefore introduce different values for β in (3.6), depending on whether we are in the expansion or in the contraction stage

$$\beta = \begin{cases} \beta_{expa} \equiv -\log(h_{max}(z)/h_{\infty,expa}) & t < t_{max} \\ \beta_{ctra} \equiv -\log(h_{max}(z)/h_{\infty,ctra}) & t > t_{max} \end{cases}. \tag{3.9}$$

Note that with this definition β_{expa} and β_{ctra} are positive quantities as for both holds $h_{\infty,expa}, h_{\infty,ctra} \gg h_{max}$. Secondly, the fact that β depends only logarithmically on h_∞ furthermore justifies approximating the time-dependent quantity $h_\infty(t)$ by its time average h_∞.

Now, to determine h_{max}, or rather the time it will take to get there from the time the disk passes at $t = t_{reach}$, we need the radial velocity of the initial expansion at $t = t_{reach}$ (see figure 10). A reasonable assumption (and similar to the proposition of Duclaux *et al.* 2007) is that the disk displaces water from underneath itself to the sides at a velocity directly proportional to its downward velocity. Therefore, we have

$$\dot{h}(t_{reach}) = \alpha_{expa} V. \tag{3.10}$$

For the velocity at the end of the contraction phase at $t_{cross} = t_{reach} + \Delta t_{expa} + \Delta t_{ctra}$, we write in a similar fashion

$$\dot{h}(t_{cross}) = -\alpha_{ctra} V. \tag{3.11}$$

Clearly, both α_{expa} and α_{ctra} are again positive quantities.

The analytical model for the radial cavity dynamics given by (3.6) and (3.8) thus has four unknown parameters α_{expa}, β_{expa}, α_{ctra} and β_{ctra}. The value of C in (3.8) follows

from the fact that the curve and its derivative in figure 10 should be continuous. We assume the collapse regime starts at the end of the contraction phase, where we have $h(t_{cross}) = h_0$ and $\dot{h}(t_{cross}) = -\alpha_{ctra} V$. From these conditions, the value of C is readily obtained,

$$C = 2h_0 \alpha_{ctra} V. \tag{3.12}$$

However, for given α_{expa}, β_{expa} and β_{ctra}, the constant α_{ctra} is also uniquely determined by the continuity of the trajectory and its derivative at $h(t_{max}) = h_{max}$, which gives

$$\alpha_{ctra} = \alpha_{expa} \sqrt{\beta_{expa}/\beta_{ctra}}\,, \tag{3.13}$$

and leaves only α_{expa}, β_{expa} and β_{ctra} to be determined.

Summarizing, the time evolution of the cavity at depth z is described by the following three equations:

$$h(z,t) = \sqrt{h_{max}^2 - \frac{gz}{\beta_{expa}}(t - t_{max})^2} \qquad \text{for } t_{reach} < t \leqslant t_{max}\,, \tag{3.14}$$

$$h(z,t) = \sqrt{h_{max}^2 - \frac{gz}{\beta_{ctra}}(t - t_{max})^2} \qquad \text{for } t_{max} < t \leqslant t_{cross}\,, \tag{3.15}$$

$$h(z,t) = \sqrt{2h_0 \alpha_{ctra} V}\sqrt{t_{coll} - t} \qquad \text{for } t_{cross} < t \leqslant t_{coll}\,, \tag{3.16}$$

where the times t_{reach}, t_{max}, t_{cross} and t_{coll} are readily related to the impact time $t = 0$ (which will be done explicitly in § 4) and h_{max} is given by

$$h_{max}(z) = h_0 \sqrt{1 + \alpha_{expa}^2 \beta_{expa} \frac{V^2}{gz}}\,, \tag{3.17}$$

as can be easily derived, e.g. from (3.14) together with its boundary conditions $h(z, t_{reach}) = h_0$ and $\dot{h}(z, t_{reach}) = \alpha_{expa} V$.

In the model described by (3.14)–(3.16) the acceleration of the cavity wall is discontinuous at, e.g. $t = t_{max}$. This reflects the fact that the acceleration in the expansion and contraction stages has been approximated by two (different) constants which can be interpreted as the time averages of the continuously changing physical acceleration of the cavity walls in the respective stages.

3.4. *Validation of the model*

We will now compare the dynamics of the radius of the void at closure depth with the theoretical prediction of (3.6) and (3.8) to validate the model and quantify the influence of the flow reversal on β_{expa} and β_{ctra}.

The parameter α_{ctra} is eliminated by relation (3.13), leaving the three parameters α_{expa}, β_{expa} and β_{ctra} to match (3.14)–(3.16) to the radial dynamics of the cavity at closure depth. Figure 13(a) shows the comparison between these fits (dashed line) and the simulations (solid line) at two different Froude numbers of 3.4 and 200. The approximation is found to be in excellent agreement throughout the collapse, faithfully reproducing the maximum expansion of the cavity and the complete time of collapse. In figure 14(a) we repeat the fitting routine described above for many Froude numbers and find the parameters α_{expa}, β_{expa} and β_{ctra} as a function of the Froude number. All are found to logarithmically depend on the Froude number (note that a logarithmic scale has been used for Fr). For completeness we also plot the derived quantity α_{ctra}, calculated from (3.13).

If in (3.14) and (3.15) the constants β_{expa} and β_{ctra} are set to 1 and therefore by (3.13), $\alpha_{ctra} = \alpha_{expa}$, we arrive at the cavity dynamics proposed by Duclaux *et al.* (2007)

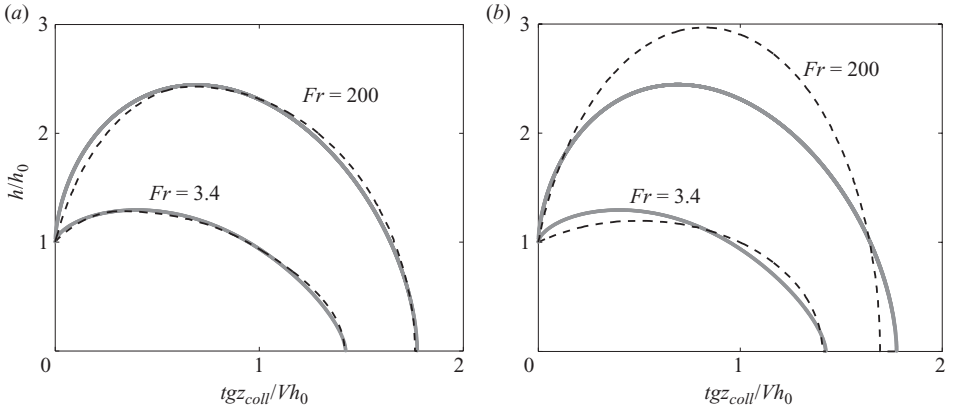

FIGURE 13. (*a*) The time evolution of the radius of the cavity at closure depth for different Froude numbers. The solid lines represent the simulation results and the dashed lines correspond to a least square fit of the approximation given by (3.14)–(3.16) with the three free parameters α_{expa}, β_{expa} and β_{ctra}. (*b*) The same numerical time evolution data as in (*a*) (solid lines) are now approximated by the model proposed by Duclaux *et al.* (2007), which consists of (3.14)–(3.15) with β_{expa} and β_{ctra} set to 1, leaving only α_{expa} as a free parameter for the least squares fit (dashed lines). In both (*a*) and (*b*) time has been rescaled by a factor gz_{coll}/Vh_0 in order to show the results for the two Froude numbers in a single plot.

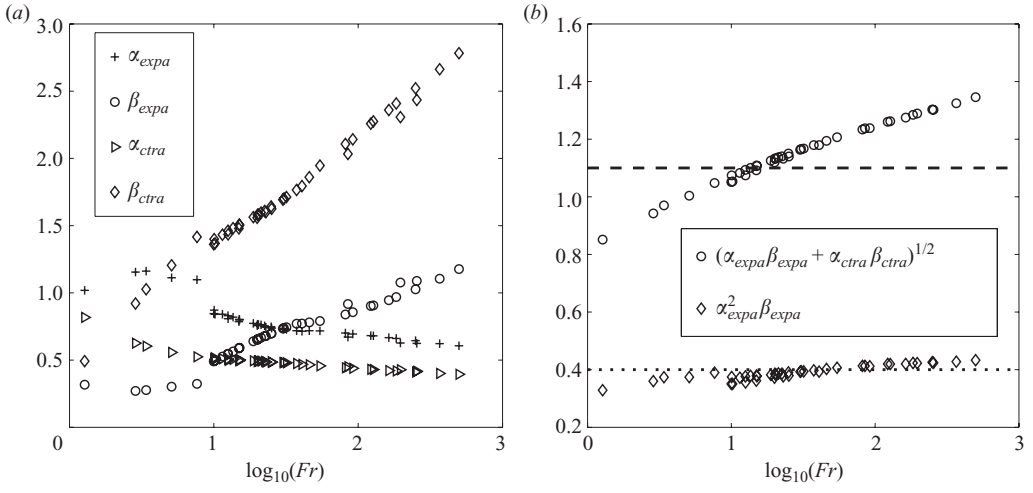

FIGURE 14. (*a*) The parameters α_{expa}, β_{expa}, α_{ctra} and β_{ctra} obtained from the fitting routine used in figure 13(*a*). All are found to logarithmically depend on the Froude number (note the logarithmic scale for *Fr*). (*b*) The quantities $\sqrt{\alpha_{expa}\beta_{expa}+\alpha_{ctra}\beta_{ctra}}$ and $\alpha_{expa}^2\beta_{expa}$ calculated from (*a*). Whereas $\sqrt{\alpha_{expa}\beta_{expa}+\alpha_{ctra}\beta_{ctra}}$ is found to weakly depend on the Froude number, $\alpha_{expa}^2\beta_{expa}$ has a nearly constant value of 0.40 (horizontal dotted line). In comparison with $\sqrt{\alpha_{expa}\beta_{expa}+\alpha_{ctra}\beta_{ctra}}$, the horizontal dashed line indicates the value $C_1 = 1.10$ obtained from the best fit to the closure depth data of figure 15.

for impacting spheres and cylinders. These dynamics are shown in figure 13(*b*) with the only free parameter α_{expa} also determined by the least square fit to the data. This approximation is seen to qualitatively reproduce the trend for the maximum expansion and collapse time, but fails to capture the exact values. It also fails to capture the

observed asymmetry in time around the maximum expansion. Our solution (3.14)–(3.15) explicitly needs not be symmetric around the maximum expansion, since it allows for different values of β at $t < t_{max}$ and $t > t_{max}$.

To conclude this section we return to the first two observations we made at the end of § 3.2 on the motion of the stagnation point and the plausible consequences for h_∞. (i) The flow reversal which occurs when the cavity starts to collapse indeed introduces an asymmetry in the behaviour around the maximum expansion. This is clearly observed in the radial dynamics of figure 13, especially for $Fr = 3.4$. (ii) As the distance of the radial flow reversal during the collapse moves away faster at higher Froude number (see figure 11*b*), we indeed have to introduce a larger h_∞^{ctra} (corresponding to a larger β_{ctra}) for higher Froude number in the fit of figure 13(*a*) to account for this effect.

4. Characteristics of the transient cavity

Now that we have derived a simplified model for the radial dynamics of the cavity, we will use it, together with the simulations and experiments, to investigate the following key characteristics of the transient cavity: (i) the depth of the pinch-off and the depth of the disk at the moment of pinch-off (§ 4.1) and (ii) the amount of air entrained through the cavity collapse (§ 4.2).

4.1. *Closure depth*

Following Glasheen & McMahon (1996), Gaudet (1998) and Duclaux *et al.* (2007) we will characterize the shape of the cavity at pinch-off by the depth of closure z_{coll}, i.e. the depth at which the pinch-off takes place. To capture more information on the full shape of the void, we will also investigate how z_{coll} relates to the total depth of the cavity $z_{disk}(t_{coll}) = z_{disk,\,coll}$ at the time of collapse (or closure) (see the inset of figure 15).

A comprehensive argument for the scaling of z_{coll} can be obtained by following a similar procedure to the one outlined in Lohse *et al.* (2004) for the determination of the closure depth after the impact of a steel ball on soft sand. The difference is that whereas in sand one can assume that due to the compressibility of the material there is hardly any outwards motion of the sand, here we are dealing with an incompressible fluid and the outward expansion of the cavity needs to be taken into account.

The time interval between impact of the disk and collapse of the cavity $\Delta t = t_{coll} - t_0$ at any depth z consists of two main parts. First, the disk needs an amount of time Δt_{reach} to reach the depth z. Second, just after the disk passes there is the time Δt_{void} it takes for the void to form, expand and collapse

$$\Delta t = \Delta t_{reach} + \Delta t_{void}. \tag{4.1}$$

The first term equals $\Delta t_{reach} = z/V$ since the velocity of the disk is constant in the experiment and simulation. In § 3 Δt_{void} was decomposed into three stages as is schematically depicted in figure 10. The collapse time can thus be written as

$$\Delta t = \Delta t_{reach} + \underbrace{\Delta t_{expa} + \Delta t_{ctra} + \Delta t_{coll}}_{\Delta t_{void}}. \tag{4.2}$$

To estimate these last three time scales at arbitrary depth z, we turn to our model for the cavity dynamics (3.14)–(3.16).

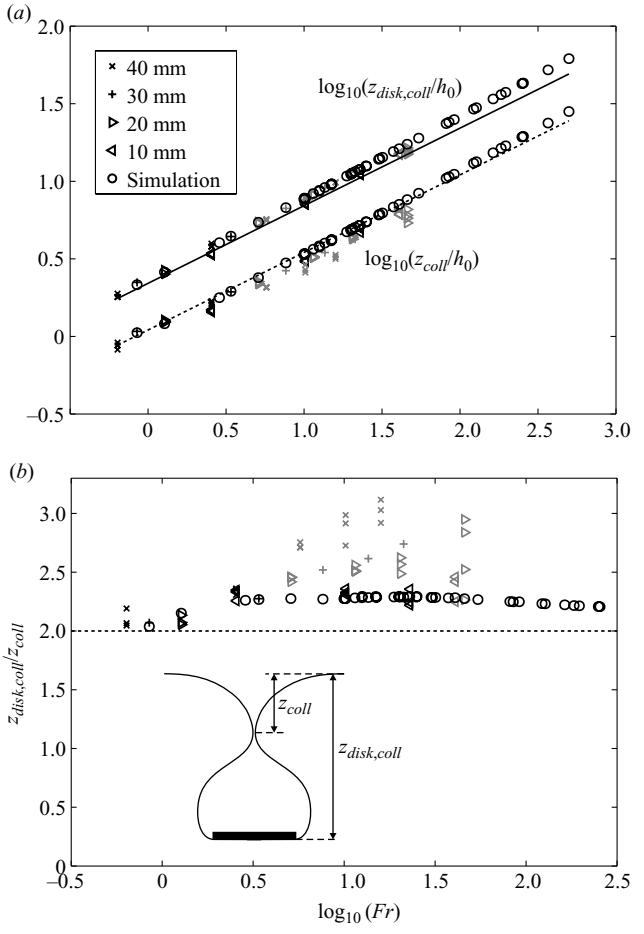

FIGURE 15. (*a*) Double logarithmic plot of the depth at which the void collapses z_{coll} and the depth $z_{disk,coll}$ of the disk at collapse time for experiments with four different disk radii and for the boundary integral simulations (open circles), all as a function of the Froude number. Experiments in which a surface seal occurs during the collapse are indicated by shaded (light grey) symbols, the experiments without a surface seal by black symbols. Here, a surface seal is said to occur if at some point in time due to air suction the splash closes onto itself and the cavity is completely sealed off. The experiments without a surface seal are found to agree well with the numerically obtained values (open circles) and the theoretical prediction for the scaling of $z_{coll}/h_0 = C_1 Fr^{1/2}$ (dashed line) and $z_{disk,coll}/h_0 = 2C_1 Fr^{1/2}$ (solid line), with $C_1 = 1.10$ obtained from a fit to the data of z_{coll}. The experiments for which a surface seal occurs are seen to slightly deviate from this prediction. The best fit of Glasheen & McMahon (1996) to their experimental data is indistinguishable from the solid line in this plot. (*b*) The ratio of the depth of the disk at the time of pinch-off $z_{disk,coll}$ and the pinch-off depth z_{coll} for different disk radii as a function of the Froude number. The experiments without a surface seal (black symbols) agree well with the numerical results (open circles). The ratio for the numerical results and experiments without a surface seal lie close to the predicted value of 2 indicated by the dashed horizontal line. The experiments in which a surface seal occurs are again indicated by the shaded (light grey) symbols and found to deviate more with increasing Froude number for a fixed disk size. The inset shows the definition of the depths z_{coll} and $z_{disk,coll}$ at the closure time.

If we combine conditions (3.10) and (3.11) with the time derivative of (3.14) and (3.15), we readily obtain

$$\Delta t_{expa} = \alpha_{expa}\beta_{expa}\frac{h_0 V}{gz}, \tag{4.3}$$

$$\Delta t_{ctra} = \alpha_{ctra}\beta_{ctra}\frac{h_0 V}{gz}. \tag{4.4}$$

Recall that $\alpha_{ctra} = \alpha_{expa}(\beta_{expa}/\beta_{ctra})^{1/2}$. The radial collapse during Δt_{coll} is in turn described by the approximation of (3.16). Since $h(t_{cross}) = h_0$ we find for this time interval

$$\Delta t_{coll} = t_{coll} - t_{cross} = \frac{1}{2\alpha_{ctra}}\frac{h_0}{V}. \tag{4.5}$$

Collecting all the above time intervals, within the model the total amount of time that passed from the impact of the disk until the collapse of the cavity at depth z is given by

$$\begin{aligned}\Delta t &= \Delta t_{reach} + \Delta t_{expa} + \Delta t_{ctra} + \Delta t_{coll} \\ &= \frac{z}{V} + (\alpha_{expa}\beta_{expa} + \alpha_{ctra}\beta_{ctra})\frac{h_0 V}{gz} + \frac{1}{2\alpha_{ctra}}\frac{h_0}{V}.\end{aligned} \tag{4.6}$$

Now, to find the closure depth z_{coll}, we need to determine at what depth the collapse will occur first, which we can do by solving

$$\frac{\mathrm{d}\Delta t}{\mathrm{d}z} = 0. \tag{4.7}$$

This gives

$$\frac{z_{coll}}{h_0} = \sqrt{\alpha_{expa}\beta_{expa} + \alpha_{ctra}\beta_{ctra}}\,Fr^{1/2}. \tag{4.8}$$

In addition, the total depth of the disk at the time of collapse, $z_{disk}(t_{coll}) = z_{disk,\,coll}$, can be obtained by substituting (4.8) into (4.6) to give $z_{disk,\,coll} = V\Delta t$, or

$$\frac{z_{disk,\,coll}}{h_0} = 2\sqrt{\alpha_{expa}\beta_{expa} + \alpha_{ctra}\beta_{ctra}}\,Fr^{1/2} + \frac{1}{2\alpha_{ctra}}. \tag{4.9}$$

When we compare these expressions with the experiments without a surface seal (black symbols) and the numerical calculations (open circles) in figure 15(*a*) we find a very good agreement with the prediction of (4.8). A fit to the data of z_{coll} gives $z_{coll}/h_0 = C_1 Fr^{1/2}$, with $C_1 = 1.10$. The agreement of the experiments in which a surface seal occurs (shaded symbols) deteriorates for a fixed disk size with increasing Froude number, since the surface seal becomes more disruptive at higher impact velocities.

In the same figure we find the experimental and numerical results for the total depth of the disk at closure $z_{disk,\,coll}$. From the observed clear power-law scaling we conclude that in the measurements we find no evidence for the constant $1/(2\alpha_{ctra})$ in (4.9). The total depth of the void is found to scale as $z_{disk,\,coll}/h_0 = C_2 Fr^{1/2}$, with $C_2 = 2.49$ close to the expected value of $C_2 = 2C_1 = 2.2$ that follows from (4.8) and (4.9). The fact that the closure depth and the total depth have the same power-law scaling $Fr^{1/2}$ indicates that the time from the initial impact of the disk to the time of closure of the cavity does not depend on the velocity of the impact, since $\Delta t = z_{disk,\,coll}/V = C_2\sqrt{h_0/g}$. Alternatively, keeping the constant term in (4.9) within the model is equivalent to keeping the last term in (4.6) and would add a $1/V$-dependence to the closure time, which vanishes for high Froude number.

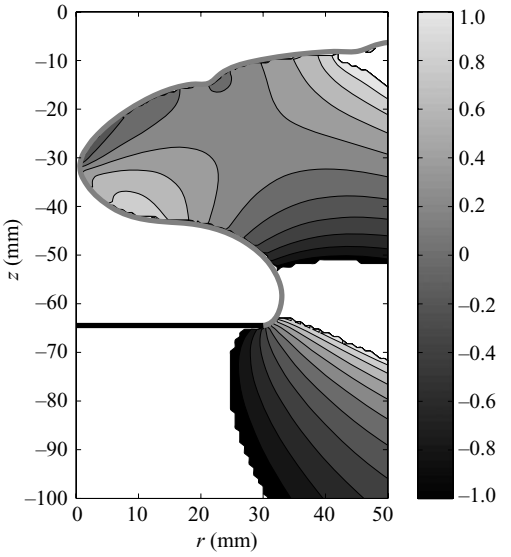

FIGURE 16. The absolute value $|v_z/v_r|$ of the ratio of the axial and radial components of the flow field, taken from the simulation at the moment of pinch-off. The disk of 30 mm radius impacts at a constant velocity of 0.5 m s^{-1} ($Fr \approx 0.8$). At this low Froude number the influence of gravity causes v_z to be of the order v_r along most of the free surface. The regions outside the cavity without any filling (the larger white areas) indicate $|v_z/v_r| > 1$.

This is in good agreement with the findings of Glasheen & McMahon (1996), who experimentally observed the same scaling for the impact of a heavy disk on a water surface with almost the same prefactor. Their result, namely $C_2 \approx 2.3$, is so close to ours ($C_2 \approx 2.2$) that their best fit to the data would be indistinguishable from our expectation as depicted in figure 15 (the solid line). The small difference may be attributed to the fact that in the case of Glasheen & McMahon (1996) the velocity is not constant during the impact and they define their Froude number with respect to the time average of this velocity. Duclaux *et al.* (2007) also found the scaling of Δt ($\propto \sqrt{h_0/g}$) for impacting spheres and furthermore reported $z_{disk,\,coll}/h_0 = 2z_{coll}/h_0 \propto Fr^{1/2}$ in agreement with our observations.

To investigate the data of figure 15(*a*) more closely it is convenient to take the ratio of $z_{coll}/z_{disk,\,coll}$ (see figure 15*b*). According to (4.8) and (4.9), this ratio should scale as

$$z_{coll}/z_{disk,\,coll} = 2 + \frac{1}{2\alpha_{ctra}\sqrt{\alpha_{expa}\beta_{expa} + \alpha_{ctra}\beta_{ctra}}} Fr^{-1/2} \approx 2 \qquad (4.10)$$

in the limit of large Froude number. In figure 15(*b*) the ratio of $z_{coll}/z_{disk,\,coll}$ in the experiments without a surface seal (black symbols) and the numerical calculations (open circles) are indeed close to the constant value of 2 (dashed black line), but at lower Froude number it decreases slightly contrary to the proposed scaling by the second term in (4.10). Although the second term of the ratio of (4.10) should become relevant when the Froude number is considerably small, this is not observed in figure 15(*b*). This can be understood by noting that in the limit of small Froude number gravity becomes more important and our assumption of non-interacting fluid layers breaks down. This is illustrated by figure 16 for $Fr = 0.85$, where v_z/v_r is found to be of order 1 along most of the free surface. This is markedly different from higher Froude numbers (see figure 9) for which the axial flow is only of the same

order around the depth of maximal cavity expansion, i.e. when and where the radial component vanishes. Thus at low Froude number the assumptions of (3.4) are violated and thus (4.10) can no longer be taken to be valid. Figure 15(*b*) also illustrates once more that the experiments with a surface seal (shaded symbols) deviate more and more from the simulations without air as the Froude number increases.

The fits to the trajectories discussed in § 3.4 provide us with the parameters α_{expa}, β_{expa} and β_{ctra} (recall that α_{ctra} is given by (3.13)), and therewith with an independent way of determining the proportionality constant $\sqrt{\alpha_{expa}\beta_{expa}+\alpha_{ctra}\beta_{ctra}}$ of (4.8). Repeating this fitting procedure for many impact velocities results in figure 14(*b*), where $\sqrt{\alpha_{expa}\beta_{expa}+\alpha_{ctra}\beta_{ctra}}$ is plotted as a function of $\log_{10} Fr$. A weak (logarithmic) dependence on the Froude number is revealed. It can also be seen that the value $C_1 \approx 1.10$ of the proportionality constant in (4.8) found from the fit to the closure depth data in figure 15 is consistent with the data when one wants to disregard the Fr dependence.

4.2. *Air entrainment*

After pinch-off, an air bubble is entrapped, as is clearly visible in figures 1(*b*) and 2. The (rescaled) volume of this bubble V_{bubble}/h_0^3 is not only found to solely depend on the Froude number, but also to exhibit close to power-law scaling behaviour. The scaling law for the volume of the bubble observed in experiment and simulation is found to be $V_{bubble}/h_0^3 \propto Fr^{\lambda}$, with $\lambda = 0.78$ (see figure 17*a*).

This is surprising, since for the impact of a liquid mass on a free surface the volume of air entrained in the process scales with a different exponent $V_{bubble} \propto Fr^{1.0}$ (Prosperetti & Oguz 1997). In this section we will try to shed light onto the origin of this scaling behaviour using our findings of § 4.1.

In § 4.1 it was found that the axial length of the enclosed bubble at pinch-off scales roughly as $(z_{coll} - z_{disk,\,coll})/h_0 \approx 1.10\,Fr^{1/2}$, if we ignore the weak-Froude-number dependence of the prefactor $\sqrt{\alpha_{expa}\beta_{expa}+\alpha_{ctra}\beta_{ctra}}$ (see figure 14*b*). Therefore, the scaling of the axial length $z_{coll} - z_{disk,\,coll}$ of the enclosed bubble cannot by itself account for the observed scaling of V_{bubble}. The radial length scale h_{rad} of the bubble must therefore be Froude number dependent and should scale as

$$\frac{h_{rad}}{h_0} \propto \left[\frac{V_{bubble}}{h_0^2(z_{disk,coll}-z_{coll})}\right]^{1/2} \propto \left[\frac{Fr^{0.78}}{Fr^{0.50}}\right]^{1/2} = Fr^{0.14}. \tag{4.11}$$

Now what would we expect based on our simplified model? The maximum radial expansion of the cavity at any depth z is given by $h_{max}(z)$ (see (3.17)). As the depth z_{max} at which the radial size of the bubble is maximal is somewhere between the closure depth z_{coll} and the depth of the disk at closure $z_{disk,\,coll}$, we have $z_{max} \approx (z_{coll} + z_{disk,\,coll})/2 = (3/2)\sqrt{\alpha_{expa}\beta_{expa}+\alpha_{ctra}\beta_{ctra}}\,Fr^{1/2}$. If we substitute this depth into $h_{max}(z)$ (3.17) we find

$$\begin{aligned} h_{rad} \propto h_{max}(z_{max}) &\approx h_0\sqrt{1+\frac{2\alpha_{expa}^2\beta_{expa}}{3\sqrt{\alpha_{expa}\beta_{expa}+\alpha_{ctra}\beta_{ctra}}}Fr^{1/2}} \\ &\approx h_0\sqrt{1+0.26\,Fr^{1/2}}. \end{aligned} \tag{4.12}$$

In the last (approximate) equation we have used that $\sqrt{\alpha_{expa}\beta_{expa}+\alpha_{ctra}\beta_{ctra}} \approx 1.10$ and $\alpha_{expa}^2\beta_{expa} \approx 0.40$ (cf. figure 14*b*). If a power-law fit h_{rad}/h_0 vs Fr is enforced on this dependence in the regime $2.5 < Fr < 250$ one obtains the observed effective exponent 0.14, i.e., $h_{rad}/h_0 \propto Fr^{0.14}$. Alternatively, by taking the square of (4.12) and

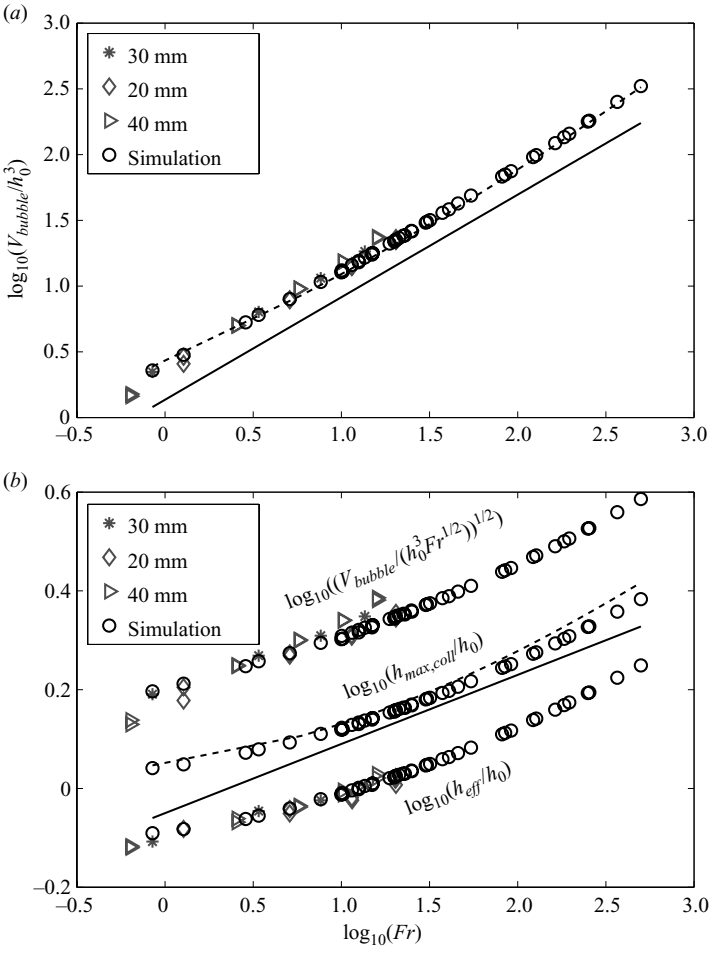

FIGURE 17. (*a*) The volume of the bubble V_{bubble} entrained during the collapse of the cavity from experiments (shaded grey symbols) and simulations (black open circles), normalized by the cubed disk radius h_0^3, as a function of the Froude number in a double logarithmic plot. The data suggest a power-law scaling $V_{bubble}/h_0^3 \propto Fr^{\lambda}$ where a linear best fit through the data between $Fr = 2.5$ and 250 gives $\lambda \approx 0.78$ (solid line, shifted for clarity). The dashed line corresponds to model prediction (4.13). (*b*) Double logarithmic plot of three quantities that measure the radial length scale of the entrapped air bubble. From bottom to top: the effective (or average) radius h_{eff} of the bubble at pinch-off (4.14), the maximum radius of the bubble $h_{max,\,coll}$ at pinch-off and the square root of the bubble volume compensated for the expected scaling of its vertical extension $[V_{bubble}/h_0 Fr^{1/2}]^{1/2}$, all compensated with the disk radius h_0. The dashed line is model prediction (4.12) and the solid line represents a power law with the scaling exponent $\lambda = 0.14$ expected from (4.11).

multiplying with the vertical extension $(z_{coll} - z_{disk,\,coll})$ of the bubble we find the following prediction for the bubble volume:

$$V_{bubble} \propto h_0^3 \left(1 + 0.26\, Fr^{1/2}\right) Fr^{1/2}\,. \tag{4.13}$$

Clearly, the model predicts power-law scaling only in the limit of large Froude numbers. Moreover, as in this limit $V_{bubble} \propto Fr$, the scaling prediction is in agreement

with the Prosperetti & Oguz (1997) result. Again, in the regime $2.5 < Fr < 250$ the effective exponent is 0.78.

We test the above prediction by looking at three different quantities that capture the radial expansion of the cavity in experiment and numerics. The first is the effective, or average, radius h_{eff} of the bubble which is computed directly from the experimental and numerical cavity profiles (i.e. without any scaling assumption of the axial length scale) at the pinch-off time by

$$h_{eff}^2 = \frac{1}{(z_{disk,\,coll} - z_{coll})} \int_{z_{disk,\,coll}}^{z_{coll}} h^2(z)\,\mathrm{d}z. \tag{4.14}$$

The second quantity we look at is the maximal radius of the bubble $h_{max,\,coll}$ at the time of pinch-off which is a more direct measure of the expansion of the cavity. $h_{max,\,coll}$ can be directly observed from the cavity profile at the time of pinch-off as the maximal radius for a depth between $z_{disk,\,coll}$ and z_{coll}.

In figure 17(b) we compare these two quantities h_{eff}/h_0 and $h_{max,\,coll}/h_0$ with a third, namely, the measured V_{bubble} compensated for the expected scaling behaviour of its axial extension $z_{disk,coll} - z_{coll} \propto h_0 Fr^{1/2}$, i.e. $V_{bubble}/h_0^3 Fr^{1/2}$. All of these three quantities follow the same trend, which is well described by prediction (4.12) from the model (the dashed line in figure 17b), and close to the expected $Fr^{0.14}$ scaling which is indicated by the solid line. Finally, comparing the measured bubble volume V_{bubble}/h_0^3 with model prediction (4.13) in figure 17(a) (dashed line), we find excellent agreement.

5. Conclusions

In this paper we investigate the purely gravitationally induced collapse of a surface cavity created by the controlled impact of a disk on a water surface. We find excellent agreement between experiments and boundary integral simulations for the dynamics of the interface, as well as for the flow surrounding the cavity. The topology and the magnitude of the flow in the simulations agree perfectly with the PIV results.

In experiments it is found that a secondary air effect, the 'surface seal', has a significant influence on the cavity shape at high Froude number. Since the surface seal phenomenon (and its influence) is more pronounced at higher impact velocities, it limits our experimental Froude number range. In the boundary integral simulations the air was intentionally excluded, thus avoiding this limitation.

Because the velocity of the impacting disk is a control parameter in our experiments, a simple theoretical argument based on the collapse of an infinite hollow cylinder describes the key aspects of the transient cavity shape.

This model accurately reproduces the dynamics of the cavity including its maximal expansion and total collapse time. It also captures the scaling for the depth of closure and the total depth of the cavity at pinch-off, and predicts their ratio to be close to 2, where 2.1 is found in experiments and simulation.

There is a close similarity of this description to the cavity dynamics proposed by Duclaux *et al.* (2007). However, by introducing the asymmetry between the radial expansion and collapse, we find a better agreement between the theory and the radial dynamics of the cavity. The fact that the flow is qualitatively different during expansion of the cavity on the one hand and its contraction on the other is found to be responsible for the asymmetry. Our approach is also conceptually different, as Duclaux *et al.* (2007) take α_{expa} to be independent of the Froude number, while we allow it to be weakly dependent on Froude and, more importantly, our description includes the last stage of the collapse, which is solely driven by inertia.

We find the volume of air entrained by the impact of the disk to behave as $V_{bubble}/h_0^3 \propto (1 + 0.26Fr^{1/2})Fr^{1/2}$. This dependence is set by the Froude dependence of two length scales, namely the axial length scale, distance between the pinch-off point and the disk, and the radial expansion of the cavity. Here we have excellent agreement between the experimental and numerical findings and the prediction of the model.

The work is part of the research program of FOM, which is financially supported by NWO. RB and SG acknowledge financial support. Furthermore, RB also acknowledges financial support from the Hans Christian Ørsted Stipend from the Technical University of Denmark.

REFERENCES

Aristoff, J. M. & Bush, J. W. M. 2009 Water entry of small hydrophobic spheres. *J. Fluid Mech.* **619**, 45–78.

Bergmann, R., Stijnman, M., Sandtke, M., van der Meer, D., Prosperetti, A. & Lohse, D. 2006 Giant bubble collapse. *Phys. Rev. Lett.* **96**, 154505/1–4.

Caballero, G., Bergmann, R., van der Meer, D., Prosperetti, A. & Lohse, D. 2007 Role of air in granular jet formation. *Phys. Rev. Lett.* **99**, 018001/1–4.

Chen, A. & Basaran, O. 2002 A new method for significantly reducing drop radius without reducing nozzle radius in drop-on-demand drop production. *Phys. Fluids* **14**, L1.

Duclaux, V., Caillé, F., Duez, C., Ybert, C., Bocquet, L. & Clanet, C. 2007 Dynamics of transient cavities. *J. Fluid Mech.* **591**, 1–19.

Fedorchenko, A. & Wang, A.-B. 2004 On some common features of drop impact on liquid surfaces. *Phys. Fluids* **16**, 1349–1365.

Gaudet, S. 1998 Numerical simulation of circular disks entering the free surface of a fluid. *Phys. Fluids* **10**, 2489–2499.

Gekle, S., van der Bos, A., Bergmann, R., van der Meer, D. & Lohse, D. 2008 Noncontinuous froude number scaling for the closure depth of a cylindrical cavity. *Phys. Rev. Lett.* **100**, 084502/1–4.

Gekle, S., Gordillo, J. M., van der Meer, D. & Lohse, D. 2009 High-speed jet formation after solid object impact. *Phys. Rev. Lett.* **102**, 034502/1–4.

Gilbarg, D. & Anderson, R. A. 1948 Influence of atmospheric pressure on the phenomena accompanying the entry of spheres into water. *J. Appl. Phys.* **19**, 127–139.

Glasheen, J. W. & McMahon, T. A. 1996 A hydrodynamic model of locomotion in the basilisk lizard. *Nature* **380**, 340–342.

de Jong, J., de Bruin, G., Reinten, H., van den Berg, M., Wijshoff, H., Versluis, M. & Lohse, D. 2006*a* Air entrapment in piezo-driven inkjet printheads. *J. Acoust. Soc. Am.* **120**, 1257–1265.

de Jong, J., Jeurissen, R., Borel, H., van den Berg, M., Wijshoff, H., Reinten, H., Versluis, M., Prosperetti, A. & Lohse, D. 2006*b* Entrapped air bubbles in piezo-driven inkjet printing: their effect on the droplet velocity. *Phys. Fluids* **18**, 121511–121517.

Le, H. P. 1998 Progress and trends in ink-jet printing technology. *J. Imag. Sci. Tech.* **42**, 49–62.

Lee, M., Longoria, R. & Wilson, D. 1997 Cavity dynamics in high-speed water entry. *Phys. Fluids* **9**, 540–550.

Liow, J.-L., Morton, D., Guerra, A. & Grey, N. 1996 Dynamics of splash formation in gas injected systems. In *Howard Worner International Symposium on Injection in Pyrometallurgy* (ed. M. Nilmani & T. Lehner), pp. 137–148.

Lohse, D., Bergmann, R., Mikkelsen, R., Zeilstra, C., van der Meer, D., Versluis, M., van der Weele, K., van der Hoef, M. & Kuipers, H. 2004 Impact on soft sand: void collapse and jet formation. *Phys. Rev. Lett.* **93**, 198003/1–4.

Morton, D., Liow, J.-L. & Rudman, M. 2000 An investigation of the flow regimes resulting from splashing drops. *Phys. Fluids* **12**, 747–763.

Oguz, H. & Prosperetti, A. 1990 Bubble entrainment by the impact of drops on liquid surfaces. *J. Fluid Mech.* **219**, 143–179.

Oguz, H. N. & Prosperetti, A. 1993 Dynamics of bubble-growth and detachment from a needle. *J. Fluid Mech.* **257**, 111–145.

Oguz, H. N., Prosperetti, A. & Kolaini, A. R. 1995 Air entrapment by a falling water mass. *J. Fluid Mech.* **294**, 181–207.

Power, H. & Wrobel, L. C. 1995 *Boundary Integral Methods in Fluid Mechanics*. WIT Press.

Prosperetti, A. 2002 *Drop Surface Interactions*. CISM Courses and Lectures No. 456. Springer.

Prosperetti, A., Crum, L. & Pumphrey, H. 1989 Underwater noise of rain. *J. Geophys. Res.* **94**, 3255–3259.

Prosperetti, A. & Oguz, H. 1997 Air entrainment upon liquid impact. *Phil. Trans. R. Soc. Lond.* A **355**, 491–506.

Rein, M. 1993 Phenomena of liquid drop impact on solid and liquid surfaces. *Fluid Dyn. Res.* **12**, 61–93.

Royer, J., Corwin, E., Flior, A., Cordero, M.-L., Rivers, M., Eng, P. & Jaeger, H. 2005 Formation of granular jets observed by high-speed X-ray radiography. *Nat. Phys.* **1**, 164–167.

Thoroddsen, S. T., Etoh, T. G. & Takehara, K. 2007 Experiments on bubble pinch-off. *Phys. Fluids* **19**, 042101–042129.

Thoroddsen, S. & Shen, A. 2001 Granular jets. *Phys. Fluids* **13**, 4–6.

Worthington, A. M. 1908 *A Study of Splashes*. Longman and Green.

Worthington, A. M. & Cole, R. S. 1897 Impact with a liquid surface, studied by the aid of instantaneous photography. *Phil. Trans. R. Soc. Lond.* A **189**, 137.